

Resonant Spin Transmission Mediated by Magnons in a Magnetic Insulator Multilayer Structure

Yabin Fan,^{*} Joseph Finley, Jiahao Han, Megan E. Holtz, Patrick Quarterman, Pengxiang Zhang, Taqiyyah S. Safi, Justin T. Hou, Alexander J. Grutter, and Luqiao Liu^{*}

While being electrically insulating, magnetic insulators can behave as good spin conductors by carrying spin current with excited spin waves. So far, magnetic insulators are utilized in multilayer heterostructures for optimizing spin transport or to form magnon spin valves for reaching controls over the spin flow. In these studies, it remains an intensively visited topic as to what the corresponding roles of coherent and incoherent magnons are in the spin transmission. Meanwhile, understanding the underlying mechanism associated with spin transmission in insulators can help to identify new mechanisms that can further improve the spin transport efficiency. Here, by studying spin transport in a magnetic-metal/magnetic-insulator/platinum multilayer, it is demonstrated that coherent magnons can transfer spins efficiently above the magnon bandgap of magnetic insulators. Particularly the standing spin-wave mode can greatly enhance the spin flow by inducing a resonant magnon transmission. Furthermore, within the magnon bandgap, a shutdown of spin transmission due to the blocking of coherent magnons is observed. The demonstrated magnon transmission enhancement and filtering effect provides an efficient method for modulating spin current in magnonic devices.

enhanced under certain temperature due to the improved spin mixing conductance.^[6,7] Besides, researchers have also shown that a NiO layer on top of topological insulator^[16] or heavy metal^[15,17] can allow transfer of spin current and result in magnetic switching through spin-orbit torque. Moreover, antiferromagnetic insulator spacers such as Cr₂O₃ and CoO have also been utilized to form magnon valve structures for switching on and off the spin current.^[9,11,12] While the spin transmission inside (anti) ferromagnetic insulators has been clearly demonstrated, there are still debates over the exact physical origin of transferred spins, whether they are mediated by magnetic resonance-induced coherent spin waves,^[18,19] thermal gradient-caused incoherent magnons,^[9,10,20,21] or by short-range magnetic fluctuations and evanescent waves.^[6,9,22] Additionally, it is unclear if the spin transmission efficiency through magnetic insulators can be optimized under certain magnon frequency and wavelength.


1. Introduction

Magnetic insulators can transfer spin information in the form of magnon spin current in the absence of Ohmic losses,^[1–3] which serves as a promising platform for realizing low-power spintronic devices and circuits.^[4,5] Recently, employing magnetic and antiferromagnetic insulators as spacers in magnetic heterostructures, researchers have demonstrated that efficient spin transmission and conversion can be realized.^[6–17] For example, it has been shown that by using a thin NiO layer as a spacer, the spin pumping signal generated from a ferromagnet can get

In this work, we study the transmission of magnon spin current in an epitaxial platinum (Pt)/yttrium-iron-garnet (YIG)/permalloy (Py) multilayer stack, where we excite nonequilibrium magnons in the top Py layer through the ferromagnetic resonance (FMR), which then transmit through an insulating YIG layer and get detected by the inverse spin Hall effect (ISHE) voltage in underlying Pt layer. We find that a resonance enhancement on spin transmission can be realized when the FMR-excited magnon frequency in Py coincides with that of the perpendicular standing spin-wave (PSSW) mode from YIG (Figure 1a-right). While in general spins can transmit through YIG via magnon flows (Figure 1a-left) over a broad range of frequencies, the enhancement of spin transmission rate under resonant frequencies can be more than ten times higher than under the nonresonant condition. By changing the magnetic field configuration, we can tune the frequency window for spin transmission enhancement, achieving a narrow-band to broadband transition as the magnon modes evolve. Moreover, we also observe a complete blockage of magnon spin transport when the microwave-excited Py magnons have a lower frequency than the magnon bandgap of YIG, which acts as a filter for magnons. Resonant enhancement and cutoff behavior in particles' transport have been known for other systems such as electrons and photons. The novel effects revealed in this work

Dr. Y. Fan, Dr. J. Finley, J. Han, P. Zhang, T. S. Safi, J. T. Hou, Prof. L. Liu
 Microsystems Technology Laboratories
 Massachusetts Institute of Technology
 Cambridge, MA 02139, USA
 E-mail: yabin_fan@hotmail.com; luqiao@mit.edu

Dr. M. E. Holtz, Dr. P. Quarterman, Dr. A. J. Grutter
 NIST Center for Neutron Research
 National Institute of Standards and Technology
 Gaithersburg, MD 20899, USA

 The ORCID identification number(s) for the author(s) of this article can be found under <https://doi.org/10.1002/adma.202008555>.

DOI: 10.1002/adma.202008555

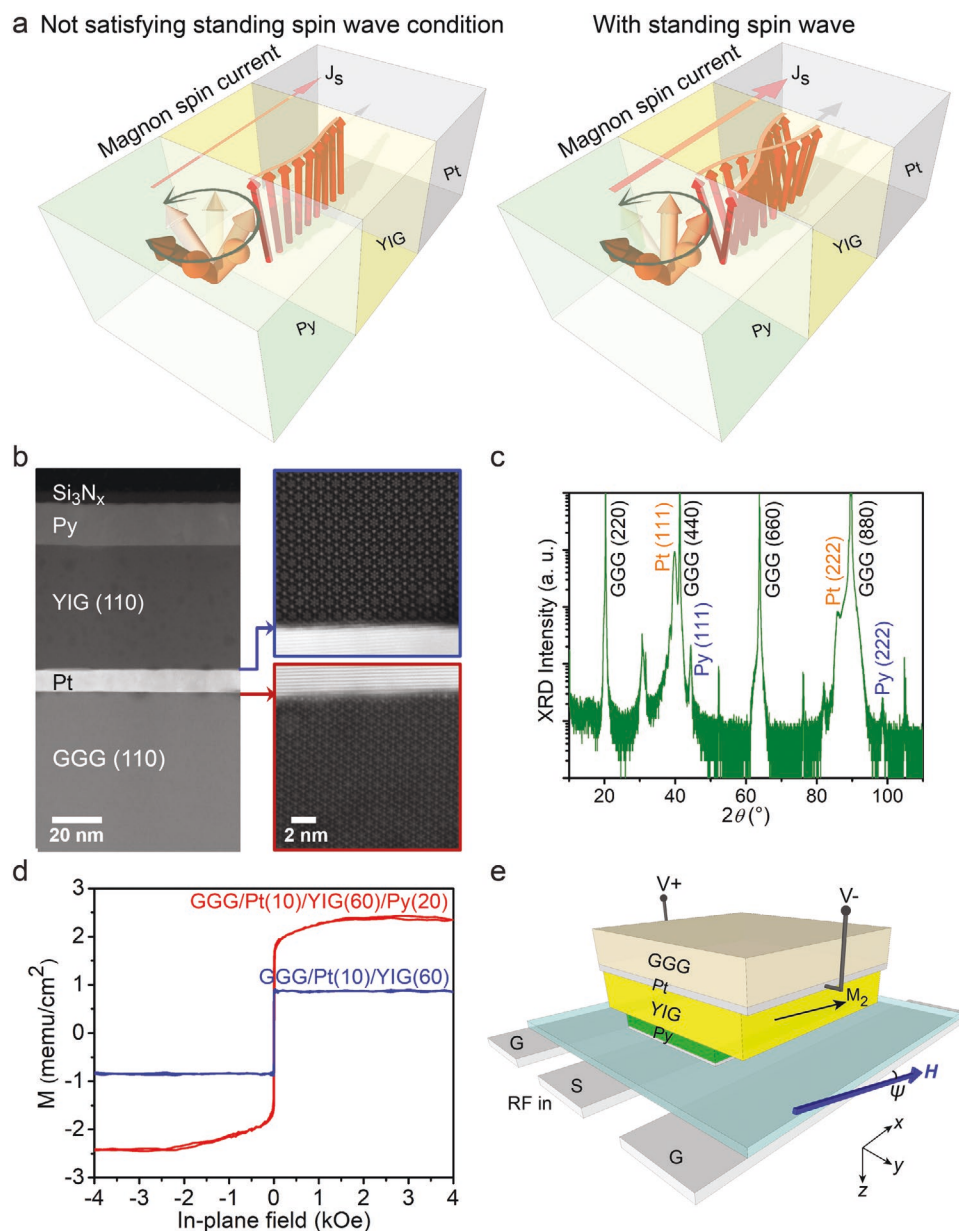


Figure 1. Structural and magnetic properties of the GGG/Pt/YIG/Py multilayer. a) Schematic of the magnon spin transmission from the Py layer to the Pt layer in the Py/YIG/Pt multilayer structure with and without the presence of PSSW in YIG. b) STEM image of the GGG/Pt(10)/YIG(60)/Py(20)/Si₃N_x(5) (unit in nm) sample. The zoom-in images show the crystalline phases near the GGG/Pt and the Pt/YIG interfaces. c) XRD measurement on the GGG/Pt(10)/YIG(60)/Py(20)/Si₃N_x(5) sample. d) VSM measurement on GGG/Pt(10)/YIG(60) and GGG/Pt(10)/YIG(60)/Py(20)/Si₃N_x(5) samples. e) Illustration of the spin pumping measurement setup and the external magnetic field configuration. ψ is the angle between the external field and the waveguide (sample) plane. M_2 is YIG layer magnetization.

on magnons can provide useful mechanisms for modulating spin current in future magnonic devices, similar to their electronic and photonic counterparts such as antireflection coatings and Fabry–Pérot cavities.

2. Results and Discussion

To explore the spin transmission from a magnetic metal through a magnetic insulator, we first deposit 10 nm Pt as the

spin detector layer on Gd₃Ga₃O₁₂ (GGG) (110) substrate by magnetron sputtering,^[23] followed by a 450 °C in situ annealing. 60 nm YIG is further deposited, followed by another annealing step in oxygen at 850 °C. Py(20 nm)/Si₃N_x(5 nm) bilayer was finally grown on top (see the Experimental Section) to form the GGG/Pt/YIG/Py/Si₃N_x heterostructure. As is verified by scanning transmission electron microscopy (STEM) and X-ray diffraction (XRD) (Figure 1b,c), the epitaxial relationship between the crystal planes of GGG (110), Pt (111), and YIG (110) are maintained in the multilayer structure. The sharp interfaces

of GGG/Pt and Pt/YIG and the nice crystalline arrangement of atoms across the stack confirm the quality of the film. The magnetic properties of the multilayer structure were characterized using vibrating sample magnetometry (VSM). The blue solid line in Figure 1d shows the magnetization curve for a sample with the bottom half stack of GGG/Pt/YIG, illustrating a typical easy-axis hysteresis loop and a saturation magnetization $M_s = 143 \text{ emu cm}^{-3}$ ($1 \text{ emu cm}^{-3} = 1 \text{ kA m}^{-1}$), close to the expected bulk value for YIG. The red line represents results from the full stack of GGG/Pt/YIG/Py/Si₃N₄. Based on the magnetic moment value, we can attribute the sharp switching near zero magnetic field of the red line to the flipping of Py layer, and the gradual increase of the magnetic moment between 0 Oe and high field to the switching of YIG layer ($1 \text{ Oe} = 79.58 \text{ A m}^{-1}$). This observed behavior indicates an antiferromagnetic interfacial exchange coupling between Py and YIG, which is consistent with previous reports on similar YIG/ferromagnetic metal (FM) bilayer structures, including our own polarized neutron reflectometry study.^[14,24,25]

The magnon spin transmission in the multilayer structure is studied using the geometry shown in Figure 1e, where two electrodes are connected to the exposed regions of the bottom Pt layer on the opposite edges. The electrically connected sample is mounted onto a coplanar waveguide with its topside down for microwave excitation of magnetic resonance (see the Experimental Section).^[18,26,27] Under a direct current (DC) magnetic field shown in the geometry of Figure 1e, the ISHE signal V_s , which is directly proportional to the magnon spin current injected to the bottom Pt layer, is detected. The DC resistance between the top Py and the bottom Pt layers is measured to be on the order of 100 MΩ over a cross-section area of $\approx 1 \text{ cm}^2$ (see Section S5, Supporting Information). The electrical isolation through the thick insulating YIG layer hence minimizes possible contributions from electrical rectification artifacts and anomalous Nernst effect in Py.^[28,29]

Figure 2a shows the spin transmission spectrum as a function of frequency f and applied field H , when H forms an angle of $\psi = 20^\circ$ with the x -axis in the xz -plane (Figure 1e). In addition to the strong signal due to the direct spin pumping from YIG uniform (or equivalently Kittel) mode, we also observed a spin transmission signal curve that can be attributed to the Py Kittel mode, which has higher resonance frequency under the same H compared with the YIG mode, due to the larger demagnetization contribution in the Kittel formula $f = \gamma \sqrt{H(H + 4\pi M_s)}$. Here γ is the gyromagnetic ratio and $4\pi M_s$ represents the demagnetization field. The detected spin signal from Py demonstrates that spin current driven by magnetic resonance in Py can propagate through the 60 nm YIG layer in the form of magnon excitation, consistent with previous spin transmission measurements with (anti)ferromagnetic insulator insertion.^[6,7,9,10,12] To further verify the nature of this transmitted spin current (coherent vs incoherent) from the Py resonance, we carry out alternating current (AC) spin pumping measurement^[30] where we detect an oscillating voltage generated on the Pt layer at the Py FMR frequency (see Section S7, Supporting Information). The existence of the AC spin pumping in the multilayer structure provides an additional evidence on the coherent transmission of magnon current in our studied sample. On top of this magnetic insulator assisted

spin signal transmission, we also observe an unexpected feature in the spectrum, i.e., the spin current signal from the Py Kittel mode V_s gets significantly enhanced under certain frequencies, as highlighted by the dashed square box in Figure 2a. The abrupt enhancement in V_s has been further verified in V_s versus H curves measured under the three specific frequencies of 6, 8.8, and 11 GHz (Figure 2b), where the V_s in the 8.8 GHz case shows a large enhancement compared with the off-peak cases of 6 and 11 GHz.

To understand the mechanism of the observed spin transmission signal enhancement, field-modulated FMR experiment was carried out by measuring the transmission spectrum of the microwave signal through the coplanar waveguide in Figure 1e (see the Experimental Section for details). As shown in Figure 2c, we can clearly see that aside from the previously identified Kittel modes from YIG and Py, there is another absorption line that is mostly parallel with the YIG Kittel mode (particularly in medium to high field range). The enhancement in the Py spin current transmission actually happens at the (avoided) crossing point between this mode and the Py Kittel mode. Previously, it was reported that because of the dipolar^[31] or exchange interactions at the FM/YIG interface, magnon–magnon coupling can happen between the FM Kittel mode and YIG PSSW mode when the two modes are degenerate, leading to level repulsions in FMR spectrum.^[24,32] The small distortion in the Py FMR spectrum at the crossing point in Figure 2c therefore reflects this magnon coupling behavior.

To quantitatively describe the spin current transmission, we extract the spin transmission voltage V_s along the Py Kittel mode in Figure 2a and plot it as a function of the driving frequency in Figure 2f, which shows an enhancement by more than ten times at the crossing point between the Py Kittel mode and the YIG PSSW mode. Here the experimental data are normalized with the absorbed RF power under each frequency to exclude possible changes in the input microwave power. While the YIG PSSW mode can be directly excited by the applied microwave and result in a spin pumping signal, in Figure 2a we can barely see any voltage coming from the YIG PSSW mode except at the mode-crossing point, suggesting that the dominant contribution of the spin current injected into Pt layer originates from Py. Moreover, we carry out spin pumping experiment on a control sample of YIG(60 nm)/Py(20 nm)/Pt(10 nm), where the sequence of YIG and Py is flipped (see Section S8, Supporting Information). Compared with our main samples, the YIG/Py/Pt sample exhibits similar magnetic excitation behaviors in the FMR measurement. However, since YIG is not placed between the Py and Pt layers, the PSSW mode no longer provides an enhancement onto the Py spin pumping signal. This result suggests that the observed effect in our main sample is not originated from simple superpositions of the two resonance modes but is consistent with the picture shown in Figure 1a right panel, where magnons generated from the Py Kittel mode propagate through the YIG layer in a resonant fashion when their frequency is close to that of magnons in the YIG PSSW mode. Previously it was observed that spin pumping signal could also be increased in the presence of magnon–photon^[33] or magnon–phonon coupling.^[34] The spin pumping enhancement exhibited in our experiment originates

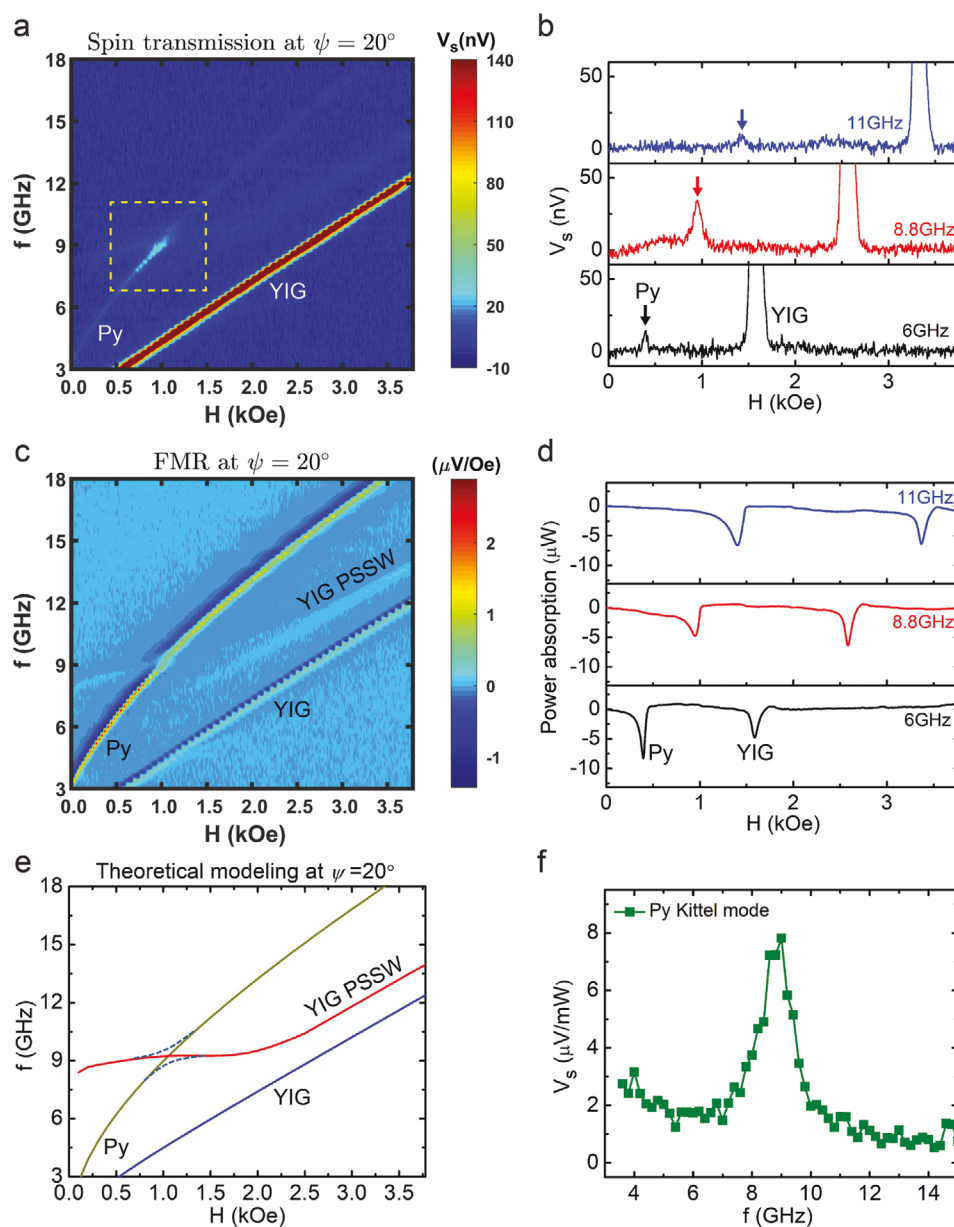


Figure 2. Spin transmission and FMR measurements of the GGG/Pt/YIG/Py sample under 20° field angle. a) Spin transmission spectrum measured by the ISHE voltage on the Pt underlayer for the GGG/Pt/YIG/Py sample. Dashed rectangular box highlights the Py spin transmission enhancement region. b) Spin voltage measured at 6, 8.8, and 11 GHz, respectively, as function of external magnetic field. Py and YIG spin signal peaks are labeled. c) Field-modulated FMR spectrum measured for the GGG/Pt/YIG/Py sample. d) The absorption of transmitted microwave power in FMR measurement at 6, 8.8, and 11 GHz, respectively, as function of external magnetic field. e) Theoretical modeling of the resonance frequency of Py Kittel mode, YIG Kittel mode, and YIG PSSW mode. Dashed curves indicate the avoid-crossing when magnon–magnon interactions are considered. f) Spin transmission voltage extracted from (a) along the curve of Py Kittel mode. V_s is normalized with the absorbed RF power.

from magnon–magnon interactions from two different layers, in contrast to the mechanisms revealed before.

In Figure 2c, we note that the f versus H curve of the YIG PSSW mode deviates from being perfectly parallel with that of the YIG Kittel mode in the low field region, which is different from the usually studied case.^[24,32,35] This deviation is related to the non-collinear arrangement between the Py and YIG magnetic moment orientations due to their different demagnetization fields. To account for this, we model the Pt/

YIG/Py multilayer structure and determine the resonance frequency for the three different modes, Py Kittel, YIG Kittel, and YIG PSSW under different applied fields (see Sections S2 and S3, Supporting Information), and the results are shown by the different curves in Figure 2e. The dashed curves close to the mode crossing region indicate the level repulsion when magnon–magnon interactions are included. It can be seen that the model agrees well with the spectrum obtained in both the spin transmission and FMR measurements.

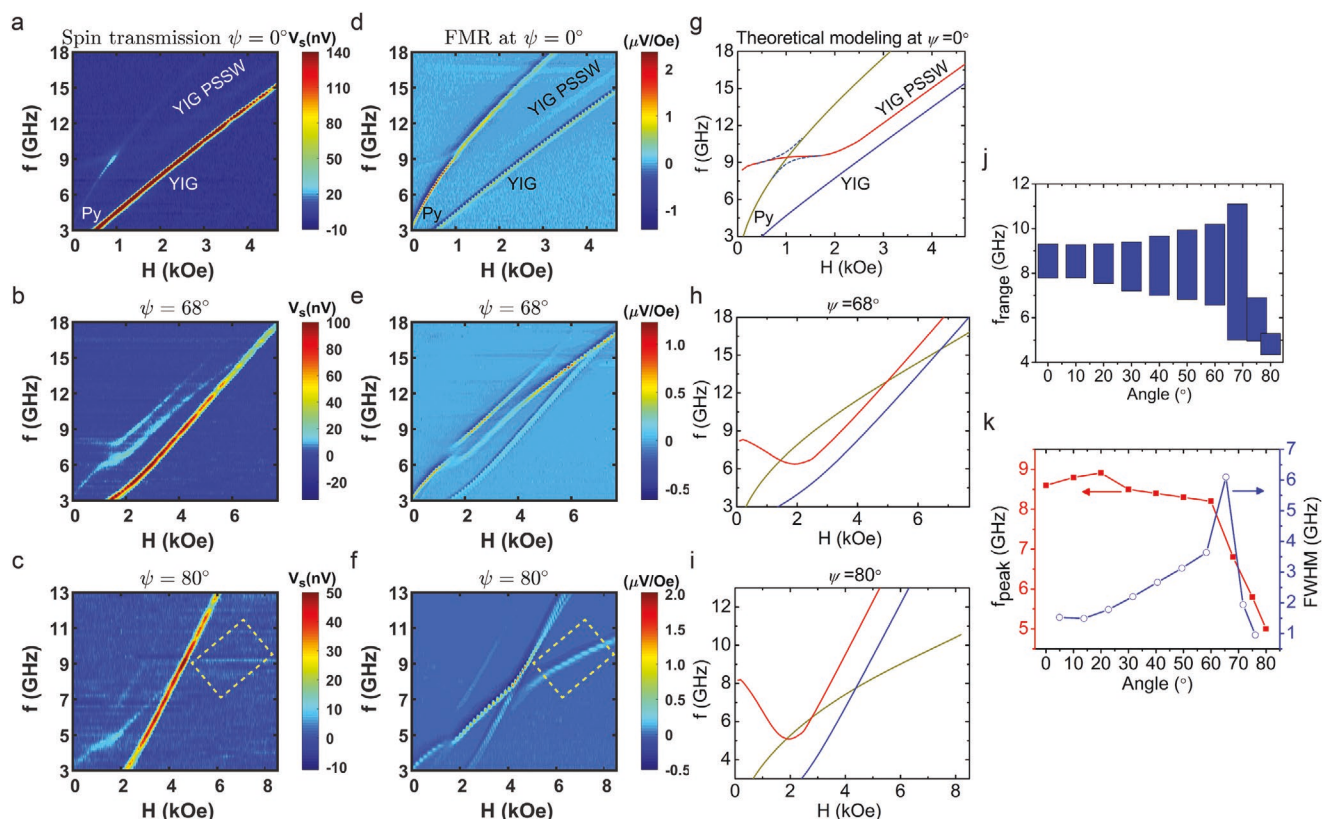


Figure 3. Spin transmission and FMR spectra under different field angles. a–c) Spin transmission spectra for $\psi = 0^\circ$, 68° , and 80° . d–f) FMR (micro-wave absorption) spectra for $\psi = 0^\circ$, 68° , and 80° . g–i) Theoretical modeling of resonance frequencies of the Py Kittel mode, the YIG Kittel mode, and the YIG PSSW mode for three different field angles. The avoid-crossing due to magnon–magnon interaction is illustrated by the dashed lines in (g) as an example. To keep figures easy to read, features of avoid-crossing are not shown in (h) and (i). j) Histogram of the frequency range under which Py spin transmission shows enhancement at different field angles. k) Peak position and linewidth of the Py spin transmission enhancement peak under different field angles.

The frequency under which the magnon transmission exhibits enhancement can be tuned by changing the magnetic field angle ψ . In **Figure 3a–c**, we show the spin transmission spectra for $\psi = 0^\circ$, 68° , and 80° , respectively. The corresponding FMR spectra and the resonance frequency determined from modeling are shown in **Figure 3d–f, g–i**. For the low angle case ($\psi = 0^\circ$ in **Figure 3a**), the Py mode and the YIG PSSW mode cross each other in a small region of frequency, leading to a narrow-band enhancement in the spin transmission spectrum. In the meantime, for $\psi = 68^\circ$ (**Figure 3b**), the Py mode and the YIG PSSW mode stay nearly degenerate over a much wider frequency range, where they form parallel hybridized modes upon consideration of magnon–magnon interactions. These hybridized modes lead to a broadband enhancement in V_s , as shown by the wide bright region. In the high angle case ($\psi = 80^\circ$, **Figure 3c**), the spin transmission enhancement reduces to narrow-band again due to the separation of the two modes in the high frequency range. Under each applied field angle, we can fit the spin transmission signal along the Py Kittel mode curve and the resultant linewidth (full width at half maximum) for $\psi = 0^\circ$ – 80° is summarized in **Figure 3j**. From the figure we observe that the bandwidth for spin transmission enhancement increases as ψ increases from 0° to 68° , and it quickly drops when ψ is above 68° . The frequency of enhancement peak

under every ψ is summarized in **Figure 3k**. It can be seen that the peak frequency can be adjusted between 9 GHz (at 0°) and 5 GHz (at 80°), providing a useful mechanism for realizing a tunable spin transmission modulator for magnons.

In **Figure 3f**, we observe that the Py Kittel mode not only couples with those from the YIG PSSW mode but can also intersect with the YIG Kittel mode as the frequency increases. Around $f = 11$ GHz, the Py and YIG Kittel modes show repulsion due to the hybridization and then separate into two branches for $f > 11$ GHz. While both of the two branches are clearly visible in the FMR spectrum of **Figure 3f**, surprisingly in the spin transmission spectrum under the same field condition, we do not detect V_s signal from the Py branch when the frequency of Py mode is lower than that of the YIG Kittel mode (see the comparison between the box regions in **Figure 3c, f**). To further verify this behavior, we carried out spin transmission and FMR measurements under another high field angle, $\psi = 75^\circ$ (**Figure 4a, b**). The corresponding theoretical resonance curves are shown in **Figure 4d**. Again, we observe that the Py spin transmission signal disappears when its frequency is lower than the YIG Kittel mode. V_s along the Py Kittel mode (dashed rectangular box) in **Figure 4a** is summarized as a function of frequency f in **Figure 4c**, which shows a sharp cut-off at the YIG FMR frequency. Via systematic power dependence

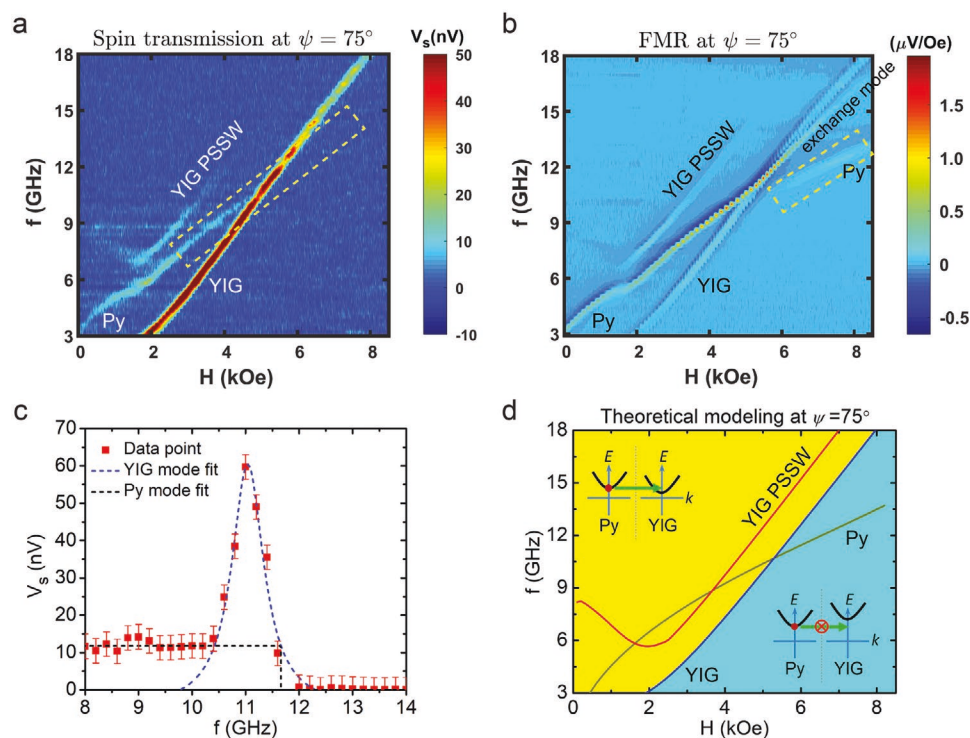


Figure 4. Cutoff of Py magnon spin current beyond YIG Kittel mode. a) Spin transmission spectrum for $\psi = 75^\circ$. The dashed rectangular box encloses the Py Kittel mode along which the V_s data are extracted and presented in (c). b) FMR spectrum for $\psi = 75^\circ$. c) The Py spin transmission voltage extracted along the mode (enclosed by the rectangular box in (a)). The dashed blue and black curves denote contributions from the YIG mode and Py mode. The error bars represent standard deviation. d) Theoretical modeling of resonance frequencies of the Py Kittel mode, the YIG Kittel mode and the YIG PSSW mode for $\psi = 75^\circ$. The insets illustrate the relative position between the Py magnon band and the YIG magnon band, as well as whether Py magnon spin current can transmit through YIG, in different regions of (f, H) space.

measurement, we demonstrate that the disappearance of the Py spin transmission signal is not caused by a weakened microwave power absorption (Section S9, Supporting Information).

The disappearance of Py spin transmission signal discussed above suggests that the spin current driven by Py magnetic resonance cannot transmit through the YIG layer in the form of coherent magnons when the magnon frequency is lower than that of the YIG Kittel mode. When considering the vertical spin transmission in the multilayer structure, the $f(H)$ curve of YIG Kittel mode separates the whole (f, H) space into two parts—above and below the YIG magnon bandgap. As is depicted in Figure 4d, in the upper-left region, the Py magnon frequency lies above the bottom of YIG magnon band (upper inset in Figure 4d), therefore the spin current can transport coherently through YIG in the form of propagating magnons. On the contrary, in the lower-right corner, since the magnons of Py Kittel mode lie within the YIG magnon bandgap (lower inset in Figure 4d), they are blocked by the YIG layer and consequently no Py spin transmission signal is detected. This spin transmission cutoff behavior suggests that coherent magnons, rather than the FMR-induced spin-Seebeck effect are responsible for the detected voltage, since a thermally driven magnon current will not have a frequency dependence but will only rely on the temperature gradient of the multilayer structure. As is shown in Figure 4b, the absorbed microwave power, hence the thermal gradient, remains finite beyond the cut-off frequency, which should not lead to the disappearance of the

Py spin transmission voltage. The steep change of the Py spin transmission voltage at the cut-off frequency also suggests that compared with possible thermally driven incoherent magnons in YIG which can exist over the whole frequency range, the transmission of magnons via coherent spin waves can be a much more efficient approach. Finally, in Figures 3f and 4b, we note that the YIG FMR peak itself splits into two narrowly separated branches, where the lower one can be identified as the exchange mode which is localized at the YIG/Py interface.^[24] With a resonance frequency lower than the Kittel mode, this lower branch does not lead to a corresponding spin pumping signal in Figures 3c and 4a, probably due to the same reason as the cutoff of Py spin pumping signal discussed above.

3. Conclusion

Our results reveal that compared with thermal magnons or magnetic fluctuations, the coherent spin wave acts as an efficient approach for transferring spin current through magnetic insulators, when the driving frequency lies above the magnon bandgap. Moreover, the PSSW mode in the magnetic insulator opens an additional channel to boost the transmission coefficient of magnon spin current in magnetic multilayers. The resonance condition for the PSSW mode can be configured via tuning the thickness of the magnetic insulator. Meanwhile, one can also modify the bandwidth for transmission enhancement

by adjusting the field angle. The demonstrated resonant transmission of spin current and filtering effect from the magnon bandgap unveil a new approach for tailoring spin transport in nanoscale structures, which can provide useful functions for spin-based information processing technologies.

4. Experimental Section

Material Growth: During the growth of the GGG/Pt(10)/YIG(60)/Py(20)/Si₃N₄(5) (unit in nm) hybrid structure, the 10 nm Pt was first grown on the GGG (110) substrate by an ultrahigh-vacuum magnetron sputtering system at room temperature, with the Ar pressure of 0.26 Pa (2 mTorr), and was subsequently annealed at 450 °C for 1 h in situ. After cooling down, a 60 nm YIG was sequentially grown on the Pt layer inside the magnetron sputtering system at room temperature, with the Ar pressure of 1.30 Pa (10 mTorr). Pt was grown by DC sputtering while YIG was grown by AC RF sputtering. After that, the GGG/Pt/YIG sample was put inside a thermal furnace for rapid thermal annealing. The annealing was carried out at 850 °C for 3 min, with an oxygen flow rate of 50 mL min⁻¹ inside. After annealing, a Ni₈₀Fe₂₀ (Py) (20 nm) layer was grown on the GGG/Pt/YIG sample inside the magnetron sputtering chamber, using DC sputtering with the Ar pressure of 0.26 Pa (2 mTorr) at room temperature. A final layer of Si₃N₄(5 nm) was grown on top of Py as the passivation layer, using AC RF sputtering with the Ar pressure of 0.26 Pa (2 mTorr) at room temperature.

STEM Measurements: Cross-sectional specimens were prepared of the GGG/Pt/YIG/Py/Si₃N₄ sample by focused ion beam lift-out using a Thermo-Fischer Nova NanoLab 600.^[36] Before lift-out, protective layers of sputtered carbon followed by ion beam deposited Pt–C were applied to the surface of the thin film. Rough milling steps were performed with 30 keV Ga⁺ ions, and the final thinning of the sample was at 5 keV to reduce surface damage.

High-resolution STEM experiments were then performed on the GGG/Pt/YIG/Py/Si₃N₄ sample by a Thermo-Fischer Titan 80–300 keV (S)TEM instrument^[36] operating with a primary beam energy of 300 keV. Annular dark-field images were acquired using a Fischione high-angle annular dark-field detector^[36] with a convergence semiangle of 13.7 mrad and inner collection semiangle of ≈60 mrad. To obtain a high signal-to-noise image with minimal scan distortions, 12–15 scans taken with a dwell time of 1 μs per pixel were acquired, aligned via cross-correlation, and averaged to form a single image. Because signal from the platinum dominates image contrast, a gamma factor of 0.5 was applied to the images for display purposes.

X-ray Diffraction Measurements: XRD was carried out on the GGG/Pt/YIG/Py/Si₃N₄ sample to determine the crystallinity of the different layers, and the result is shown in Figure 1c. To obtain the XRD spectra, a Rigaku SmartLab^[36] with a Cu Kα source was used and the measurement has covered a wide-angle range (2θ from 10° to 110°). Additionally, a Ni filter was used to filter out the Cu Kβ line. Due to the close lattice constant matching between the YIG layer and the GGG substrate, the broad YIG peaks are almost perfectly overlapped with strong and sharp peaks from the GGG such that they appear as a shoulder feature on either side of the GGG peaks. Four main Bragg peaks of YIG and GGG are observed: (220), (440), (660), and (880), which suggest the (110) growth orientation of the YIG layer.^[37,38] At 2θ = 39.7°, a new peak is observed besides the YIG (440), which belongs to the 10 nm Pt layer with (111) texturing and finite thickness fringes associated with this peak are observed. This observation is consistent with previous reports on similar structures.^[37,38] At 2θ = 44.5° and 98.7°, peaks are observed that correspond to the Py layer with (111) texture, which is further indicative of high structural quality and epitaxial nature of the sample.

Spin Pumping and FMR Measurements: For the spin-pumping experiment, a 5 mm × 5 mm GGG/Pt(10 nm)/YIG(60 nm) sample was first prepared using the method discussed above. Then, a shadow mask was utilized to grow 2 mm × 2 mm

Py(20 nm)/Si₃N₄(5 nm) in the central area of the GGG/Pt/YIG sample. To expose the Pt in the edge area of the sample to make contacts, another mask was used to cover the central region of the sample and etched the YIG away in the side area. To further isolate the Pt (and the silver paste used for making contacts) from the Py layer, a thin square-shape Scotch tape was put on top of the Py(20 nm)/Si₃N₄(5 nm) to fully cover it. The sample was mounted onto a coplanar waveguide to carry out the spin-pumping experiment, as shown in Figure 1e. The RF microwave was generated by an RF signal generator (Giga-tronics 12000A) and was sent into the waveguide through a coaxial cable. The signal generator output power (17 dBm) was modulated by a lock-in amplifier (by 80% modulation-depth), and the spin-pumping voltage was measured by the same lock-in amplifier.^[28,39]

In the FMR experiment, a constant RF signal (17 dBm) was sent into the waveguide. An electromagnetic coil was used to generate the AC modulating magnetic field, as shown in Figure S1 of the Supporting Information. The electromagnetic coil was driven by an AC power supply that was synchronized with the lock-in amplifier oscillator output. An RF diode was connected with the other end of the waveguide (see Figure S1, Supporting Information). The voltage was measured by the same lock-in, which reflects the field-modulated microwave absorption signal when the magnetic sample is in the resonance state. The whole waveguide and the modulation coil were placed in the center of the electromagnet pole gap, where static magnetic field was applied during the measurement.

Supporting Information

Supporting Information is available from the Wiley Online Library or from the author.

Acknowledgements

The authors acknowledge support from AFOSR under Award No. FA9550-19-1-0048, National Science Foundation under Award No. ECCS-1808826, and from SMART, one of seven centers of nCORE, a Semiconductor Research Corporation program, sponsored by National Institute of Standards and Technology (NIST). P.Q. acknowledges support from the National Research Council Research Associateship Program. The authors also acknowledge research performed in part at the NIST Center for Nanoscale Science and Technology.

Conflict of Interest

The authors declare no conflict of interest.

Data Availability Statement

The data that support the findings of this study are available from the corresponding author upon reasonable request.

Keywords

coherent spin wave transport, magnetic insulators, magnon spin current, resonant spin transmission

Received: December 18, 2020

Revised: February 15, 2021

Published online: April 25, 2021

- [1] A. V. Chumak, V. I. Vasyuchka, A. A. Serga, B. Hillebrands, *Nat. Phys.* **2015**, *11*, 453.
- [2] Y. Kajiwara, K. Harii, S. Takahashi, J. Ohe, K. Uchida, M. Mizuguchi, H. Umezawa, H. Kawai, K. Ando, K. Takanashi, S. Maekawa, E. Saitoh, *Nature* **2010**, *464*, 262.
- [3] L. J. Cornelissen, J. Liu, R. A. Duine, J. B. Youssef, B. J. van Wees, *Nat. Phys.* **2015**, *11*, 1022.
- [4] V. V. Kruglyak, S. O. Demokritov, D. Grundler, *J. Phys. D: Appl. Phys.* **2010**, *43*, 264001.
- [5] A. Khitun, M. Bao, K. L. Wang, *J. Phys. D: Appl. Phys.* **2010**, *43*, 264005.
- [6] H. Wang, C. Du, P. C. Hammel, F. Yang, *Phys. Rev. Lett.* **2014**, *113*, 097202.
- [7] C. Hahn, G. de Loubens, V. V. Naletov, J. Ben Youssef, O. Klein, M. Viret, *EPL (Europhys. Lett.)* **2014**, *108*, 57005.
- [8] W. Lin, K. Chen, S. Zhang, C. L. Chien, *Phys. Rev. Lett.* **2016**, *116*, 186601.
- [9] Z. Qiu, J. Li, D. Hou, E. Arenholz, A. T. N'Diaye, A. Tan, K.-i. Uchida, K. Sato, S. Okamoto, Y. Tserkovnyak, Z. Q. Qiu, E. Saitoh, *Nat. Commun.* **2016**, *7*, 12670.
- [10] Q. Li, M. Yang, C. Klewe, P. Shafer, A. T. N'Diaye, D. Hou, T. Y. Wang, N. Gao, E. Saitoh, C. Hwang, R. J. Hicken, J. Li, E. Arenholz, Z. Q. Qiu, *Nat. Commun.* **2019**, *10*, 5265.
- [11] Z. Qiu, D. Hou, J. Barker, K. Yamamoto, O. Gomonay, E. Saitoh, *Nat. Mater.* **2018**, *17*, 577.
- [12] J. Cramer, F. Fuhrmann, U. Ritzmann, V. Gall, T. Niizeki, R. Ramos, Z. Qiu, D. Hou, T. Kikkawa, J. Sinova, U. Nowak, E. Saitoh, M. Kläui, *Nat. Commun.* **2018**, *9*, 1089.
- [13] H. Wu, L. Huang, C. Fang, B. S. Yang, C. H. Wan, G. Q. Yu, J. F. Feng, H. X. Wei, X. F. Han, *Phys. Rev. Lett.* **2018**, *120*, 097205.
- [14] Y. Fan, P. Quarterman, J. Finley, J. Han, P. Zhang, J. T. Hou, M. D. Stiles, A. J. Grutter, L. Liu, *Phys. Rev. Appl.* **2020**, *13*, 061002.
- [15] T. Moriyama, S. Takei, M. Nagata, Y. Yoshimura, N. Matsuzaki, T. Terashima, Y. Tserkovnyak, T. Ono, *Appl. Phys. Lett.* **2015**, *106*, 162406.
- [16] Y. Wang, D. Zhu, Y. Yang, K. Lee, R. Mishra, G. Go, S.-H. Oh, D.-H. Kim, K. Cai, E. Liu, S. D. Pollard, S. Shi, J. Lee, K. L. Teo, Y. Wu, K.-J. Lee, H. Yang, *Science* **2019**, *366*, 1125.
- [17] H. Wang, J. Finley, P. Zhang, J. Han, J. T. Hou, L. Liu, *Phys. Rev. Appl.* **2019**, *11*, 044070.
- [18] Y. Tserkovnyak, A. Brataas, G. E. W. Bauer, *Phys. Rev. Lett.* **2002**, *88*, 117601.
- [19] R. Khymyn, I. Lisenkov, V. S. Tiberkevich, A. N. Slavin, B. A. Ivanov, *Phys. Rev. B* **2016**, *93*, 224421.
- [20] S. M. Rezende, R. L. Rodríguez-Suárez, A. Azevedo, *Phys. Rev. B* **2016**, *93*, 054412.
- [21] K. Chen, W. Lin, C. L. Chien, S. Zhang, *Phys. Rev. B* **2016**, *94*, 054413.
- [22] M. Dąbrowski, T. Nakano, D. M. Burn, A. Frisk, D. G. Newman, C. Klewe, Q. Li, M. Yang, P. Shafer, E. Arenholz, T. Hesjedal, G. van der Laan, Z. Q. Qiu, R. J. Hicken, *Phys. Rev. Lett.* **2020**, *124*, 217201.
- [23] H. Chang, T. Liu, D. R. Hickey, P. A. P. Janantha, K. A. Mkhoyan, M. Wu, *APL Mater.* **2017**, *5*, 126104.
- [24] S. Klingler, V. Amin, S. Geprägs, K. Ganzhorn, H. Maier-Flaig, M. Althammer, H. Huebl, R. Gross, R. D. McMichael, M. D. Stiles, S. T. B. Goennenwein, M. Weiler, *Phys. Rev. Lett.* **2018**, *120*, 127201.
- [25] Y. Li, W. Cao, V. P. Amin, Z. Zhang, J. Gibbons, J. Sklenar, J. Pearson, P. M. Haney, M. D. Stiles, W. E. Bailey, V. Novosad, A. Hoffmann, W. Zhang, *Phys. Rev. Lett.* **2020**, *124*, 117202.
- [26] E. Saitoh, M. Ueda, H. Miyajima, G. Tatara, *Appl. Phys. Lett.* **2006**, *88*, 182509.
- [27] H. L. Wang, C. H. Du, Y. Pu, R. Adur, P. C. Hammel, F. Y. Yang, *Phys. Rev. B* **2013**, *88*, 100406.
- [28] L. Bai, P. Hyde, Y. S. Gui, C. M. Hu, V. Vlaminck, J. E. Pearson, S. D. Bader, A. Hoffmann, *Phys. Rev. Lett.* **2013**, *111*, 217602.
- [29] A. Azevedo, L. H. Vilela-Leão, R. L. Rodríguez-Suárez, A. F. Lacerda Santos, S. M. Rezende, *Phys. Rev. B* **2011**, *83*, 144402.
- [30] M. Weiler, J. M. Shaw, H. T. Nembach, T. J. Silva, *Phys. Rev. Lett.* **2014**, *113*, 157204.
- [31] C. Liu, J. Chen, T. Liu, F. Heimbach, H. Yu, Y. Xiao, J. Hu, M. Liu, H. Chang, T. Stueckler, S. Tu, Y. Zhang, Y. Zhang, P. Gao, Z. Liao, D. Yu, K. Xia, N. Lei, W. Zhao, M. Wu, *Nat. Commun.* **2018**, *9*, 738.
- [32] H. Qin, S. J. Hämmäläinen, S. van Dijken, *Sci. Rep.* **2018**, *8*, 5755.
- [33] L. Bai, M. Harder, Y. P. Chen, X. Fan, J. Q. Xiao, C. M. Hu, *Phys. Rev. Lett.* **2015**, *114*, 227201.
- [34] H. Hayashi, K. Ando, *Phys. Rev. Lett.* **2018**, *121*, 237202.
- [35] J. Chen, C. Liu, T. Liu, Y. Xiao, K. Xia, G. E. W. Bauer, M. Wu, H. Yu, *Phys. Rev. Lett.* **2018**, *120*, 217202.
- [36] Certain commercial equipment, instruments, or materials are identified in this paper to foster understanding. Such identification does not imply recommendation or endorsement by the National Institute of Standards and Technology, nor does it imply that the materials or equipment identified are necessarily the best available.
- [37] M. Aldosary, J. Li, C. Tang, Y. Xu, J.-G. Zheng, K. N. Bozhilov, J. Shi, *Appl. Phys. Lett.* **2016**, *108*, 242401.
- [38] M. Evelt, C. Safranski, M. Aldosary, V. E. Demidov, I. Barsukov, A. P. Nosov, A. B. Rinkevich, K. Sobotkiewicz, X. Li, J. Shi, I. N. Krivorotov, S. O. Demokritov, *Sci. Rep.* **2018**, *8*, 1269.
- [39] Y. Fan, J. T. Hou, J. Finley, S. K. Kim, Y. Tserkovnyak, L. Liu, *Appl. Phys. Lett.* **2019**, *115*, 172405.